Approach to optimize 3-dimensional brain functional activation image with high resolution: a study on functional near-infrared spectroscopy

ZESHAN SHOAIB, M. AHMAD KAMRAN, M. M. N. MANNAN, AND MYUNG YUNG JEONG[*]

Department of Cogno-Mechatronics Engineering, Pusan National University, San 30 Jangjeon-dong Geumjeong-gu, Busan 609-735, South Korea
[*]*myjeong@pusan.ac.kr*

Abstract: In this study, 3-dimensional (3-D) enhanced brain-function-map generation and estimation methodology is presented. Optical signals were modelled in the form of numerical optimization problem to infer the best existing waveform of canonical hemodynamic response function. Inter-channel activity patterns were also estimated. The estimation of activation of inter-channel gap depends on the minimization of generalized cross-validation. 3-D brain activation maps were produced through inverse discrete cosine transform. The proposed algorithm acquired significant results for 3-D functional maps with high resolution, in comparison with that of 2-D functional *t*-maps. A comprehensive analysis by exhibiting images corresponding to several layers has also been appended.

1. Introduction

Optical brain imaging (OBI) has been situated into a favourable position among other neuroimaging modalities because it is an effective, painless, and economical way for measuring/examining the functionality of the human brain [1–3]. It provides functional information on the human brain up to a certain level that used to be possible only through invasive methodologies [4–7]. Near-infrared spectroscopy (NIRS) is an emerging neuroimaging modality under the umbrella of OBI techniques. Jobsis [8] presented the possibility of examining the oxygen level of human brain tissue by utilizing near infrared (NIR). Nowadays, this concept has grown into the form of functional near-infrared spectroscopy (fNIRS). In such systems, NIR light is thrown on the surface of head by a source optode. These light photons then travel through the scalp, skull, and different brain layers. These photons are either absorbed or scattered or reflected back, depending on the attributes of different brain layers. The absorption of these NIR light photons depend on two important chromophores in the blood, namely, oxyhaemoglobin (HbO_2) and deoxyhaemoglobin (Hb) [9]. Modified Beer–Lambert law (MBLL) is utilized to estimate the relative concentration changes of HbO_2 and Hb in a specific brain area [10,11]. Advanced fNIRS systems, like frequency and time-domain instruments, have the ability to determine the absolute changes of HbO_2, Hb, and total haemoglobin (HbT) [12]. The ease of applying an fNIRS probe has also enabled us to perform a wide variety of experiments on human adults, animals, and infants [13–15]. It is usual practice to configure a source–detector pair 1–4 cm apart, depending on the nature of experiment [16]. The source–detector configuration is very important for analysing the activation area up to a certain resolution but is constrained by the number of available source–detector optodes.

fNIRS systems may have several advantages, but at the same time, they also have some limitations. These limitations include limited spatial resolution, modest penetration depth, hair absorption, physiological noises, and motion artefacts [17–19]. The limited spatial resolution of

an fNIRS system, which is in the scale of centimetres, is due to several factors [20]. The general perception is that spatial resolution is proportional to half of the width of the source–detector separation (i.e., a few centimetres) [19,21]. A higher spatial resolution for any neuroimaging instrument is required in different fields of science and medicine [3].

Several different types of fNIRS systems have been developed to date. Initially, Jobsis's conception led to the development of continuous-wave (CW) fNIRS system [22–24]. These CW systems cannot absolutely determine the concentration changes of HbO_2 and Hb, which is their major drawback, in addition to their modest penetration depths and hypersensitivity to superficial layers [25]. To overcome these limitations, time-resolved and frequency-domain systems, which enable us to determine the absolute concentration changes of HbO_2 and Hb, were developed. Time-resolved systems use picosecond pulses of NIR light photons, which pass through layers of human brain. Because a time gap is given so that all photons are received by a nearby detector [26,27], the time resolutions of these systems are relatively poor. Additionally, while these systems inherently result in a deeper penetration of NIR light photons and better spatial resolution, there are also various limitations, for example, huge size, higher cost, and low speed. These limitations, especially the huge size, constrain time-resolved systems from being frequently used in laboratory experiments [25]. The demand for such systems in clinical applications is high, and therefore, researchers are developing and optimizing the design of such systems, so that they may become portable and have high temporal resolution. Frequency-domain devices, on the other hand, use modulated frequency and relative change in intensity and phase shift to determine the nature of activation [24,28]. These systems likewise have certain disadvantages: the penetration depth is low, quantification of optical parameters is not attainable, and experimentation is relatively difficult [25]. Although there are several hurdles that need to be addressed, fNIRS is still in a favourable position among other neuroimaging modalities.

In the past, various methodologies to enhance the spatial resolution and to minimize the depth error in constructed images have been presented. A comprehensive approach for minimizing the depth errors in diffuse optical tomography's (DOT) reconstruction is to apply a spatially variant regularization parameter [29–31]. Another approach is depth-compensated optical imaging, which modifies the depth variant sensitivity matrix directly rather than modifying the regularization parameter [32]. Spatial resolution is a discremental feature of neuroimaging modalities. The enhancement of spatial resolution enables better localization of neural activity. For instance, EEG has low-source-localization problems. A frequently used program, LORETA, connects 10–20 and 10–10 standard positions to the Talairach coordinate system [33]. These approaches could possibly enhance the spatial resolution up to a few centimetres. High-density diffuse optical tomography (HD-DOT) has a much better spatial resolution. The first experimentally resolved OBI data reconstruction in HD-DOT has a spatial resolution in the order of several millimetres [34]. Additionally, Yamamoto et al. [35] reported that high-density probe arrangement can effectively enhance the spatial resolution and discussed the effect of fibre arrangement on the extent of absorption change calculated via conventional mapping methodology. Several other researchers have presented empirical and simulation results obtained by addressing the issue of spatial resolution of the fNIRS system [18,36,37]. Among these approaches, bundled approaches have attracted several researchers with improved results. In such schemes, multiple sources are placed a few millimetres apart to increase the number of channels that enhance the spatial resolution [38].

OBI systems provide functional information of the path between source and detector, but it is a usual practice to relate this information with the midpoint. Thus, the information related to other points in the path and/or the points in between two channels cannot be estimated. In other words, we can say the configuration of OBI systems has a constraint in that these midpoints cannot be estimated directly. In addition to this, trial-to-trial variability in measured data is still a bottleneck that needs to be addressed. The extensive use of OBI systems is possible if an appropriate

methodology that can estimate inter-point activation through filling these gaps is developed. At the same time, it is important to remove/understand the root cause of trial-to-trial variability. Some past studies have presented algorithms that can estimate activity at unknown gaps [3,39], such as empirical orthogonal function [40] and singular spectrum analysis [41,42]. However, these methods have some advantages and disadvantages with certain constraints. Therefore, an algorithm or methodology that can estimate a full 4-D (i.e., 3-D spatial and time) spatio-temporal map on activation points of the source–detector pair and other unknown points between these points is required. However, a methodology with such properties has not been reported until now. In this study, we demonstrate a methodology that can estimate such maps with 3-D spatial information and at each sample time.

2. Materials and methods

2.1. Participants

In this study, a group of 9 healthy participants (6 male, 3 female) with a mean age of 30 (range: 20 to 45) years were examined. The criteria for selection were as follows:

- All right-handed participants with no former and present neuronal (based on the system check list 90-R) and grievous internal disorder (as specified by self-assessment) were included.

- Participation was after discussion with their guardians and experimental team.

- No pregnancies were diagnosed in the female participants.

- Subjects were also rewarded financially for their inclusion.

The study was accomplished in manners conforming to the latest version of the Declaration of Helsinki, and the study was approved by the National Research Ethics Committee (Pusan National University).

2.2. Task

For this study, each control subject visited the lab where the experiment was performed. At the commencement of the experimentation, the participants were acquainted with the experiment process and with the directives. The experiment was composed of 5 blocks of activity, separated by 30 s of rest in between. In the resting periods, the participants were directed to sit motionless and relax. For activity sessions, they were directed to tap their right index finger for 10 s in a pleasant rhythm. Moreover, a 10 s baseline was added before the first task segment (Fig. 1).
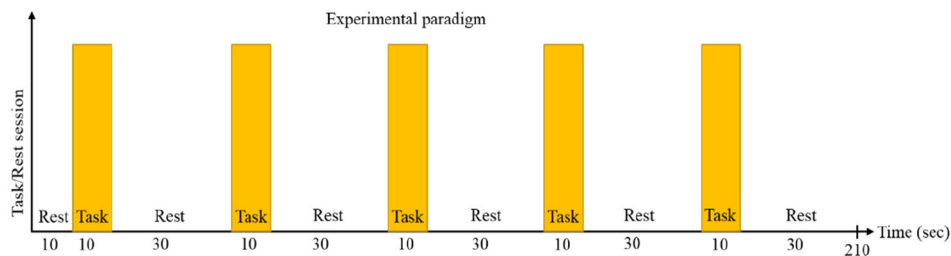

Fig. 1. One complete dataset over a span of 210 s, consisting of six rest periods and five task periods detected by fNIRS from C3 region of brain. First rest period was 10 s and the remaining were of 30 s each. Yellow blocks represent 10 s activity periods. The x- and y-axes show time (in seconds) and activation, respectively.

The subjects were not told about the durations of the task and rest sessions. They were advised to listen for an alarm and to watch out for a visual display that indicates the start and end of the task session. By doing this, the subjects have to be attentive throughout the experiment without feeling any habituation. In addition, visual monitoring of each subject is done to make sure that each subject has performed all tasks and rest sessions properly. Each participant was positioned on a comfortable chair with head rest in a dark room, and a load of optic fibres was supported with a hook attached to an fNIRS system. The experiment was a finger-tapping task, and subjects were advised not to have any unrequired motions, to avoid motion artefacts. The subjects were hairless or had very short and straight hair. Mathematically, each activity period can be equated with a rectangular provoked wave, the extent of which is zero during rest and one during activity. We used such provoked rectangular waves to analyse phase synchronization and coherence between the haemoglobin and provoked signals.

2.3. Instrumentation

The fNIRS signal was inscribed with a multi-channel NIRS system equipped with 32 optodes (fibre optic probes). Each optode can even be used as a source and as a detector. The device ejects light at 2 different wavelengths: 760 nm and 830 nm. One source and 24 detectors were placed on each subject's skull in the left motor cortex, according to the International 10–20 system, with each detector receiving light from one light source. The path between each detector and source is termed as an independent channel. We used 2.5 cm source–detector distance in the first layer and a distance of 0.5 cm between succeeding detectors. There were 24 channels (characterized by source–detector distances of 2.5 cm, 3 cm, and 3.5 cm): (1, 13, 4, 16, 7, 19, 10, 22), (2, 14, 5, 17, 8, 20, 11, 23), and (3, 15, 6, 18, 9, 21, 12, 24), respectively, in the left hemisphere, with their positions illustrated in Fig. 2. The dataset for each channel contains about 380 time-points, corresponding roughly to 210 s. The sampling frequency was 1.81 Hz. The optodes were set using the wave guard cap and secured using a dedicated black fabric cap.

2.4. Reconstruction of haemodynamics from optical data

The fundamental property during interaction between tissues and light is absorption. This phenomenon of light absorption by the brain tissues is modelled by the Beer–Lambert law and mathematically written as

$$I_\lambda = I_{\lambda_0} \times e^{-\mu_a^\lambda \times L_\lambda}, \tag{1}$$

where I_λ is the detected intensity, I_{λ_0} is the initial intensity, μ_a^λ is the absorption coefficient, and L_λ is the differential path length. However, the absorption coefficient is not sufficient for describing the attenuation of light intensity in case of cortical interactions. Because cortical tissues are a highly scattered medium of NIR light, a second coefficient, μ_s^λ, called a scattering coefficient, is then introduced. The Beer–Lambert law defined in Eq. (1) is then written as follows:

$$I_\lambda = I_{\lambda_0} \times e^{-(\mu_a^\lambda + \mu_s^\lambda) \times L_\lambda}. \tag{2}$$

Chromophore concentrations are fundamentally known to change with respect to time in biological tissues because of blood flow. Thus, for each instant t_n, the Beer–Lambert Eq. (2), called modified Beer–Lambert law (MBLL) [22], can be written as follows:

$$I_\lambda(t_n) = I_{\lambda_0} \times e^{-([c(t_n)] \times \varepsilon_\lambda \times d \times L_\lambda + G)}, \tag{3}$$

where scattering contribution $\mu_s^\lambda \times L$ has been grouped into the term G, ε_λ is the extinction coefficient of blood tissue, and the differential path length factor d has been used to measure the certain possibility that photons travel paths that are longer than the separation of the source–detector pair because they diffuse multiple times inside the medium, with a small amount
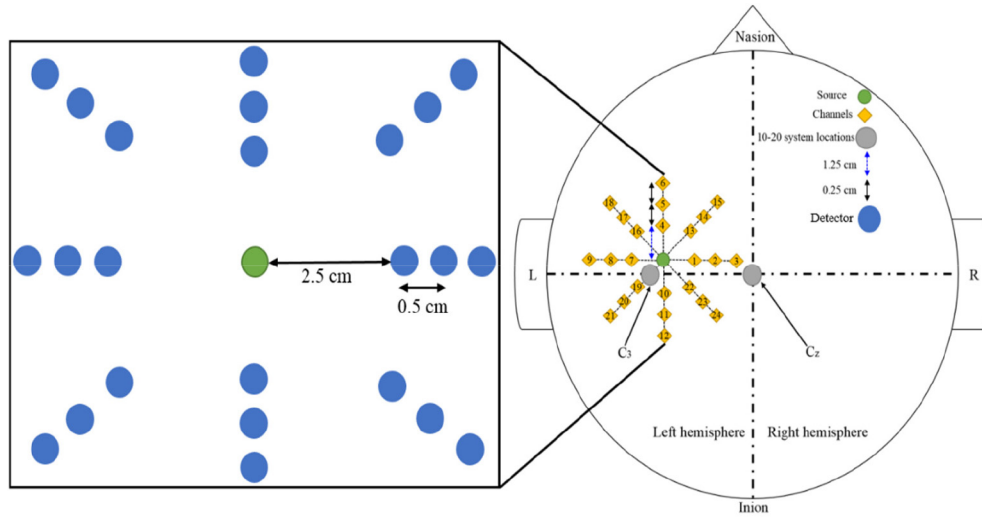
Fig. 2. Green circle represents the source, yellow squares represent 24 channels (with respective numbers), and grey circles represent reference points. The channels are defined as the midpoint of the source from each detector. The optodes were set on the subject's left hemisphere using C_3 and C_z of the International 10–20 system as the reference points. The distance of the eight nearest detectors from the source and the distance between the detectors are indicated by blue and black lines, respectively. The magnified part on the left side illustrates the actual detectors (blue circles) and source (green circle) that form the yellow channels for measurement.

reaching up to the detector. Thus, we can write the modified Beer–Lambert Law in Eq. (3) as follows:

$$A^\lambda = \ln\left(\frac{I_{\lambda_0}}{I_\lambda}\right) = [c(t_n)] \times \varepsilon_\lambda \times d \times L_\lambda + G, \tag{4}$$

where A^λ is the optical density. It can also be written as

$$\Delta A^\lambda = [\Delta c(t_n)] \times \varepsilon_\lambda \times d \times L_\lambda + G. \tag{5}$$

Considering two different chromophore concentrations to change (HbO_2 and Hb) at two different wavelengths λ_1, and λ_2 and the scattering term G to be constant, we obtain

$$\Delta A^{\lambda_j} = [\varepsilon_{HbO_2}^{\lambda_j}\Delta HbO_2 + \varepsilon_{Hb}^{\lambda_j}\Delta Hb] \times d \times L_{\lambda_j} + G, \tag{6}$$

where $j = 1$ and 2, and $\varepsilon_{HbO_2}^{\lambda_j}$ and $\varepsilon_{Hb}^{\lambda_j}$ are the extinction coefficients of HbO_2 and Hb, respectively.

Rewriting Eq. (6) for each wavelength, i.e., λ_1 and λ_2, we now have

$$\begin{cases} \Delta A^{\lambda_1} = [\varepsilon_{HbO_2}^{\lambda_1}\Delta HbO_2 + \varepsilon_{Hb}^{\lambda_1}\Delta Hb] \times d \times L_{\lambda_1} + G \\ \Delta A^{\lambda_2} = [\varepsilon_{HbO_2}^{\lambda_2}\Delta HbO_2 + \varepsilon_{Hb}^{\lambda_2}\Delta Hb] \times d \times L_{\lambda_2} + G \end{cases}. \tag{7}$$

Being a linear system of two equations with two unknowns, the system can be easily solved using simple linear algebra. The rearrangement of system of Eq. (7) through algebra results in the

following:

$$\Delta HbO_2(t_n) = \frac{\left(\varepsilon_{HbO_2}^{\lambda_1} \frac{\Delta A^{\lambda_2}(t_n)}{L_{\lambda_2}}\right) - \left(\varepsilon_{Hb}^{\lambda_2} \frac{\Delta A^{\lambda_1}(t_n)}{L_{\lambda_1}}\right)}{d(\varepsilon_{Hb}^{\lambda_1} \times \varepsilon_{HbO_2}^{\lambda_2} - \varepsilon_{Hb}^{\lambda_2} \times \varepsilon_{HbO_2}^{\lambda_1})} \tag{8}$$

and

$$\Delta Hb(t_n) = \frac{\left(\varepsilon_{HbO_2}^{\lambda_2} \frac{\Delta A^{\lambda_1}(t_n)}{L_{\lambda_1}}\right) - \left(\varepsilon_{Hb}^{\lambda_1} \frac{\Delta A^{\lambda_2}(t_n)}{L_{\lambda_2}}\right)}{d(\varepsilon_{Hb}^{\lambda_1} \times \varepsilon_{HbO_2}^{\lambda_2} - \varepsilon_{Hb}^{\lambda_2} \times \varepsilon_{HbO_2}^{\lambda_1})}, \tag{9}$$

where $\Delta HbO_2(t_n)$ and $\Delta Hb(t_n)$ are relative concentration changes of HbO_2 and Hb, respectively, t_n is the discrete time, and $\Delta A^{\lambda_1}(t_n)$ and $\Delta A^{\lambda_2}(t_n)$ are the optical density variations at t_n-th sample time with particular wavelengths λ_1, and λ_2, respectively.

2.5. Removal of systemic physiological signal interference

Conventionally, it is presumed that haemodynamic changes related to cortical activation contain certain physiological signals. Previous studies have demonstrated that the systemic physiological signal from superficial layers can exponentially attenuate the NIR light emitted from the source. The major contributors responsible for physiological intervention include heartbeat, respiration, low-frequency oscillations including Mayer waves, and task-related changes in systemic physiology. The raw data of CW-fNIRS have shown that, even under resting conditions, optical signals have trial-to-trial variability [43,44]. This variation could be observed between intra-subject and inter-subject trial repetitions. These variations cause fluctuations and unrepeatability in measured haemodynamic response in the different brain regions, excluding the cerebrospinal fluid (CSF), and are generally categorized into two types. The first are fluctuations whose conventional patterns are systemic and that are associated with periodic physiological activities, such as arterial pulse oscillations (~1 Hz) and respiration rhythm (0.2–0.3 Hz). The second are relatively low-frequency waves (frequency < 0.05 Hz), of which the temporal pattern has a different profile in each brain region. Both the faster and the slower variations of the Hb oxygenation state sometimes have amplitudes comparable to those of the signals evoked by functional activity. Thus, it is very important to determine these physiological signals, so that they can be carefully removed. The cardiovascular pulsation, especially, generates fast-oscillating waves, which are definitely different from the signal generated as a result of the task and can be filtered out through specific blockers/filters. Similarly, respiration rhythm could be easily removed in case the task during experimentation does not contribute much to variation of respiration frequency. The high-pass and low-pass filtering of fNIRS data are possible through NIRS-SPM software [45] with cut-off frequencies of 0.01 Hz and 0.15 Hz, respectively. Some researchers have shown that bandpass filters of bandwidth [0.6–2.0] Hz for cardiac pulsation, [0.15–0.4] Hz for respiration artefacts, and [0.05–0.2] Hz for low-frequency noise can be used [46]. Another possible way is to define a cost function composed of periodic regressors that need to be estimated, in addition to the evoked response, as described in Eq. (13). Nelder–Mead simplex iterations are later applied to estimate the amplitudes and frequencies of periodic waves that exist in measured data. In this study, we have implemented methods described in Kamran et al. [47,48] and mentioned in this manuscript in equations (10–14).

2.6. Haemodynamic response function

The most crucial part is the modelling of evoked response related to task–rest sessions. A canonical haemodynamic response model is usually used to represent impulse response. The canonical haemodynamic response function (cHRF) is composed of three gamma functions: the first representing main peak of response, the second representing post-stimulus undershoot

[49], and the third to representing early deoxygenation that is reported in several studies in past [50–52]. Consequently, the mathematical form of cHRF is as follows:

$$h(t_n) = \frac{t_n^{\alpha_1-1} \times \beta_1^{\alpha_1} \times e^{-\beta_1 t_n}}{\Gamma(\alpha_1)} - \frac{t_n^{\alpha_2-1} \times \beta_2^{\alpha_2} \times e^{-\beta_2 t_n}}{6\Gamma(\alpha_3)} - \frac{t_n^{\alpha_3-1} \times \beta_3^{\alpha_3} \times e^{-\beta_3 t_n}}{8\Gamma(\alpha_3)}, \tag{10}$$

where h is the cHRF, α_1, α_2, and α_3 are the delays of the response, undershoot, and initial dip, respectively, β_1, β_2, and β_3 are the dispersions of the response, undershoot, and initial dip, respectively, and Γ represents the gamma distribution. To evaluate the predicted response related to a particular experimentation, cHRF is convolved with experimental paradigm into

$$\tilde{y}_{Hbo_2}(t_n) = a_0 + a_1[h(t_n) * u(t_n)], \tag{11}$$

where $\tilde{y}_{Hbo_2}(t_n)$ is the haemodynamic response function (HRF), u is a function describing the onset of activity and rest sessions, and a_0 and a_1 are the base line and activity strength parameters, respectively.

2.7. Neural activation model: a formulation

Task-related activations are constructed as original time courses ΔHbO_2 of fNIRS channels $y^i_{Hbo_2}(t_n)$, $i = 1, 2, \ldots \ldots, 24$ (i represents the channel number) as $y^i_{Hbo_2}(t_n) = \tilde{y}^i_{Hbo_2}(t_n) + \gamma^i(t_n)$, where

$$\gamma^i(t_n) = a_c \sin(2\pi f_c t_n) + a_r \sin(2\pi f_r t_n) + a_m \sin(2\pi f_m t_n) + \varepsilon^i(t_n), \tag{12}$$

where $y^i_{Hbo_2}(t_n)$ is the measured HbO_2 time series at ith channel, a_c, a_r, a_m, f_c, f_r, f_m are the amplitudes and the frequencies, respectively, of the cardiac, respiratory, and Mayer waves, respectively, and $\varepsilon^i(t_n)$ is the zero-mean Gaussian noise. Because fNIRS signal measured through any region of brain has trial-to-trial variability and also varies among subjects, the neuro-activation process is therefore formulated in the form of a cost function [50] as

$$J = \sum_{n=1}^{N} [y^i_{Hbo_2}(t_n) - \{\tilde{y}^i_{Hbo_2}(t_n) + \gamma^i(t_n)\}]^2. \tag{13}$$

The variables in the model have been constrained between upper and lower values, so that the algorithm can also detect the variability among subjects and inter-task activations.

$$\left.\begin{array}{ll} 2 \le \alpha_1 \le 10, & 0 \le a_c \le 2 \\ 6 \le \alpha_2 \le 20, & 1 \le \alpha_3 \le 3 \\ 0 \le a_r \le 2, & 0.2 \le \beta_1 \le 2 \\ 0 \le \beta_2 \le 1.5, & 0.9 \le \beta_3 \le 2.9 \\ 0 \le a_m \le 2, & 0.5 \le f_c \le 1.5 \\ 0 \le a_0 \le 20, & 0.2 \le f_r \le 0.3 \\ 0 \le a_1 \le 15, & 0.09 \le f_m \le 0.1 \end{array}\right\}. \tag{14}$$

The optimal values of the free parameters (α^*_1, α^*_2, β^*_1, β^*_2, a^*_o, a^*_1, a^*_c, a^*_m, a^*_r, f^*_c, f^*_r, f^*_m) are estimated using an improved version of the simplex method, later named as Nelder–Mead simplex method (NMSM). The iteration of NMSM comprises three major steps, namely, ordering, centroid, and transformation. The details about the algorithm can be found in [53,54].

2.8. Functional brain maps and statistical significance

The estimation of functional activation and its localization from measured optical data comprises an additional challenge due to physiological and systemic noises plus trial-to-trial variability. Therefore, parameters are allowed to obtain variable values depending on the signal acquired. Let us suppose the optimal values of the parameters are found through the algorithm stated in the previous section, such that, mathematically,

$$y_{Hbo_2}^{i^*}(t_n) = a_0^* + a_1^*[h(t_n) * u(t_n)] + a_c^* \sin(2\pi f_c^* t_n) + a_r^* \sin(2\pi f_r^* t_n)$$
$$+ a_m^* \sin(2\pi f_m^* t_n) + \varepsilon^i(t_n). \tag{15}$$

The parameter a_1^* is known as activity strength parameter, and it constitutes the strength of the haemodynamic response function. It is quite logical that larger values of a_1^* indicate higher functional activity, whereas null values of a_1^* represent no activation. Similarly, negative values of a_1^* indicate deoxygenation states. It is important to verify the obtained results through statistical measure [55]. To achieve that, let us define a null hypothesis:

$$H_0 : a_1^* = 0. \tag{16}$$

The corresponding t-value with p-value < 0.01 is obtained as follows:

$$t_{value} = \frac{a_1^* - 0}{SE(a_1^*)}, \tag{17}$$

where SE is the standard error of the estimated coefficient.

2.9. Estimation of inter-channel gap's activation

In fNIRS data analysis, it is more important to exploit the particulars from both temporal and spatial variabilities to anticipate the missing values. Here, we consider the following model for oxy-fNIRS signal:

$$y_{Hbo_2}^{i(N)}(x_i, y_i, z_i, t_n) = y_{Hbo_2}^{i^*}(x_i, y_i, z_i, t_n) + \Lambda^i(x_i, y_i, z_i, t_n), \tag{18}$$

where $\tilde{y}_{Hbo_2}^{i^*}(x_i, y_i, z_i, t_n)$ is the optimal estimated activation, and $y_{Hbo_2}^{i(N)}(x_i, y_i, z_i, t_n)$ is the real neuronal activation-related signal with $\Lambda^i(t_n)$ Gaussian noise, which has a very low amplitude, given that $\tilde{y}_{Hbo_2}^{i^*}(x_i, y_i, z_i, t_n)$ represents the optimal activation signal. Because of this Gaussian noise, it could still have a certain mismatch with the actual haemodynamic response. As an optional step, it is passed through a minimizing criterion that balances the fidelity of $y_{Hbo_2}^{i(N)}(x_i, y_i, z_i, t_n)$, if it exists [56].

Let us define a norm representing residual of sum of squares of optimal HRF and mismatch of the actual neuronal-related response, as follows:

$$F[y_{Hbo_2}^{i^*}(x_i, y_i, z_i, t_n)] = ||y_{Hbo_2}^{i^*}(x_i, y_i, z_i, t_n) - y_{Hbo_2}^{i(N)}(x_i, y_i, z_i, t_n)||^2,$$
$$+ s\nabla^2[y_{Hbo_2}^{i^*}(x_i, y_i, z_i, t_n)] \tag{19}$$

where $|| \quad ||$ is the Euclidean norm, ∇^2 is the Laplace operator (penalty term) that reflects the missing values of the signal, and s is a real positive scalar that controls the degree of measuring the best estimate of $y_{Hbo_2}^{i^*}(x_i, y_i, z_i, t_n)$, and

$$P[y_{Hbo_2}^{i^*}(x_i, y_i, z_i, t_n)] = ||Dy_{Hbo_2}^{i^*}(x_i, y_i, z_i, t_n)||^2, \tag{20}$$

where D is a diagonal square matrix defined in [56]. From the aforementioned equations, minimization of fidelity $F[y_{Hbo_2}^{i^*}(x_i, y_i, z_i, t_n)]$ defined in Eq. (19) gives the following system that

allows the determination of the best estimated value:

$$[I_q + sD^T D]y_{Hbo_2}^{i*}(x_i, y_i, z_i, t_n) = y_{Hbo_2}^{i(N)}(x_i, y_i, z_i, t_n), \tag{21}$$

where I_q is the $q \times q$ identity matrix, and D^T is the transpose of D. To solve this equation, we diagonalize D by using eigenvalue decomposition [57], which results in the following eigenvalues of $D : v_i = -2 + 2 \cos \left[\frac{\pi(i-1)}{n} \right]$. Thus, Eq. (21) becomes:

$$y_{Hbo_2}^{i*}(x_i, y_i, z_i, t_n) = UXU^T y_{Hbo_2}^{i(N)}(x_i, y_i, z_i, t_n), \tag{22}$$

where X is a diagonal matrix defined as

$$X = \left\{ \begin{array}{ll} 0, & nondiagonal\ elements \\ \left(1 + s \sum_{i=1}^{3} \left(-2 + 2 \cos \left[\frac{\pi(i-1)}{n} \right] \right)^2 \right), & diagonal\ elements \end{array} \right\}. \tag{23}$$

Here, we can say U and U^T are discrete cosine and inverse cosine transform matrices [57], respectively. In 2012, Wang et al. [58] analysed that the parameter s is the degree of smoothness. It is found that a small value of s could reduce the effect of smoothness. The authors further analysed that a high value of s results in larger global error and loss of high-frequency components. The best value of s can be evaluated through generalized cross-validation (GCV) method [59,60]:

$$GCV(s) = \frac{q \left[||\tilde{y}_{Hbo_2}^{i}(x_i, y_i, z_i, t_n) - y_{Hbo_2}^{i}(x_i, y_i, z_i, t_n)||^2 \right]}{[q - Tr(H)]^2}, \tag{24}$$

where $H(s) = (I_q + sD^T D)^{-1}$ and Tr is the matrix operation trace.

3. Results

Figure 1 presents the experimental paradigm in detail. The task sessions are highlighted with yellow bars. The duration of each task session is 10 s, which is then followed by a 30 s rest session. Five trials of coupled task–rest sessions are performed, with initial rest of 10 s. Thirty seconds of rest session is chosen to ensure that no activity-related haemodynamic response remains in the HbO_2 signal.

The total time of experiment was approximately 4 min, and this did not result in any feelings of headache for any subject. The details of optode configuration and localization are shown in Fig. 2. In this experiment, a single source is used with 3 layers of rectangularized detector positions with spacings of 0.5 cm between them. Therefore, the channels are formed with source–detector separations of 2.5 cm, 3 cm, and 3.5 cm. Each layer contains 8 detectors, and therefore 24 channel locations are scanned for right-index-finger-tapping task. The left hemisphere around C_3 (International 10–20 system) is scanned at 24 sparse locations to comprehensively analyse the task-related haemodynamic response. Figure 3 presents the generic schematic of the study. fNIRS signals are measured from the nine subjects. Measured optical data are a linear combination of hemodynamic signals, physiological noises, and certain artefacts. The artefacts and unwanted noises have been removed through NIRS-SPM software and method described in Kamran et al. [47,61]. The optimal activity-related signal is then fed into the inter-channel gap's estimation, and multi-layered 3-D activation patterns are determined and shown.

Figure 4 visualizes the conventional *t*-maps (in reference to Eqs. (16) and (17)) related to the strength of activity. Because the signals are observed at 24 sparse locations, 24 locations of activity patterns have therefore been displayed in each subfigure of Fig. 4. There are no data available in between and around those channels, and therefore most of the area has no activity
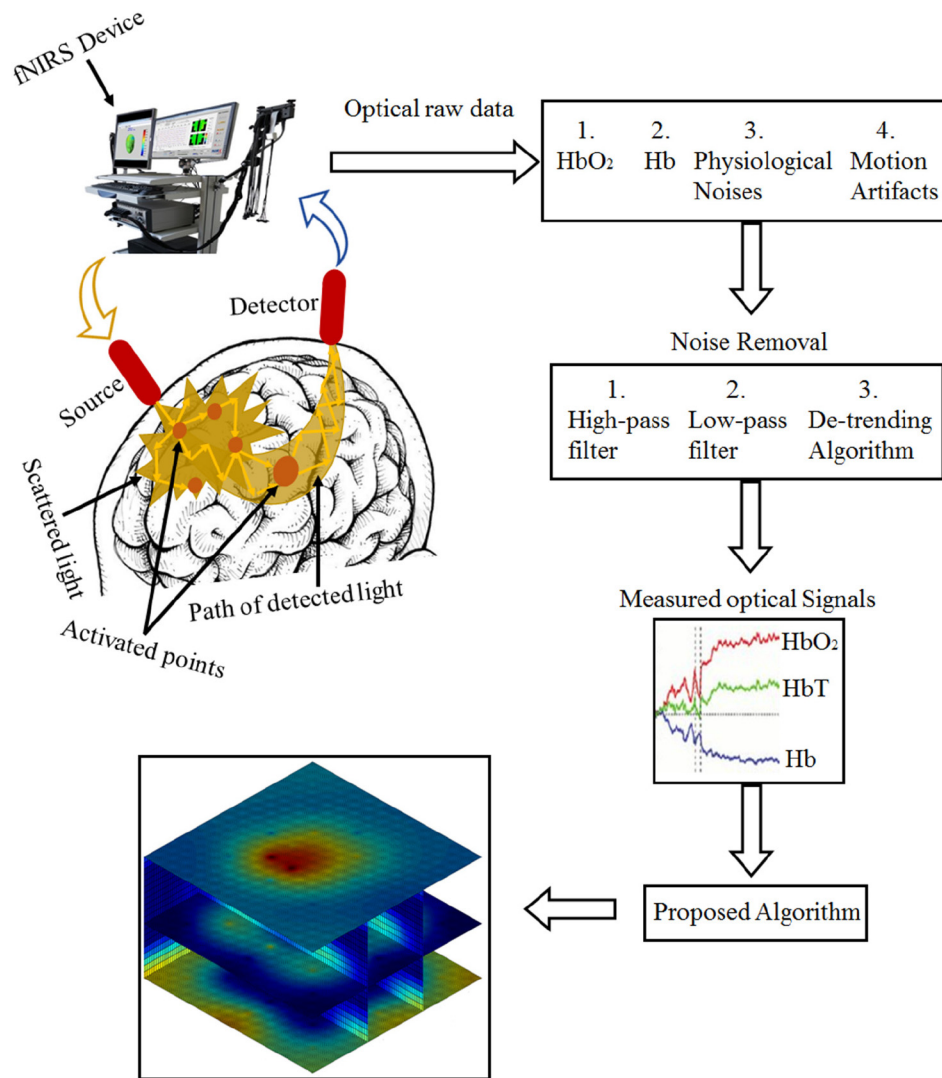
Fig. 3. Schematic of study: The complete process, from travelling of NIR light photons (with physical behaviour of scattering and absorption in brain) to generation of 3-D high-quality brain images, with slices, by the proposed algorithm. The processing steps of fNIRS data acquisition and physiological noise removal for extracting optimal oxygenation signals have also been illustrated.

information. To determine these inter-channel locations, the easiest way is to calculate the weighted average of a specific activity pattern, depending on the locations. The corresponding maps with weighted average are shown in Fig. 5. It is very important point to observe that there is no depth information in these maps either evaluated via conventional methodology (Fig. 4) or determined through further processing, i.e., weighted average (Fig. 5). The rest-related functional brain maps are shown in Fig. 6. It is evident from this figure that almost all of the area is inactivated, because the motor-related channels have shown no activity and inter-channel locations already have no data. To determine the best fit of HRF from pre-processed optical data, the data are fed through the optimization algorithm presented in Eq. (15). In this algorithm, each

parameter of cHRF defined in Eq. (10) is allowed to be free. The algorithm chooses the best value of these parameters, depending on the minimum error found in each step of iteration.
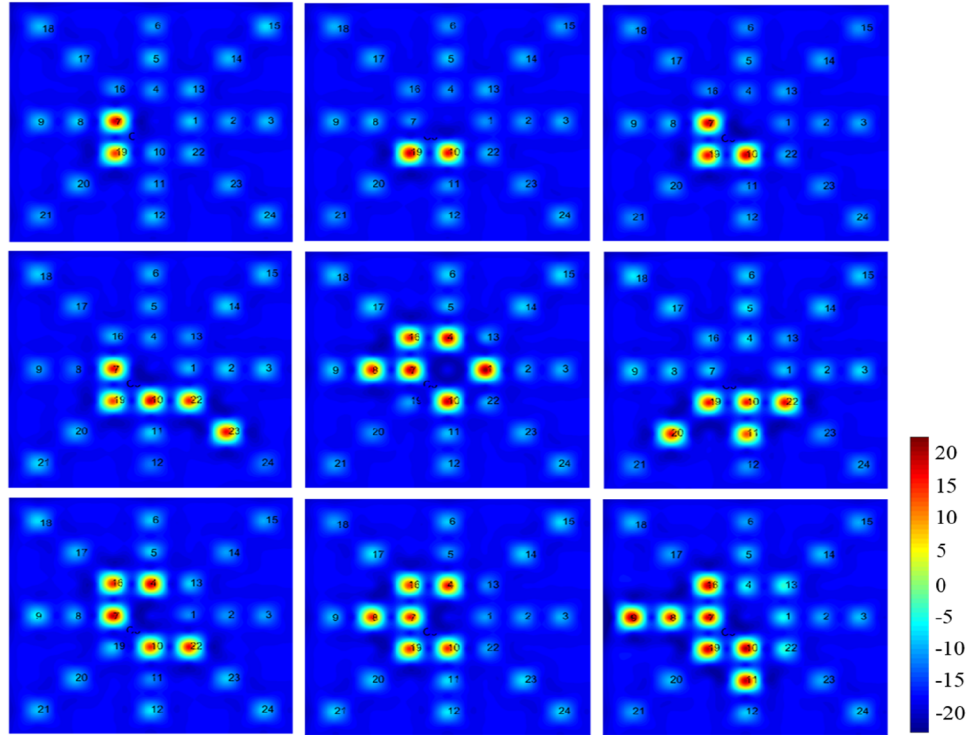

Fig. 4. Statistical t-maps of brain activation (without averaging) with fNIRS during finger-tapping task for all subjects (left to right, respectively). The red-coloured circles show the significantly active channels while relatively close to blue-coloured circles, which show deactivated channel locations. The channel numbers are also displayed at each location. The colour bar (at the bottom-right) shows activity strength.

Figure 7 presents the results for the 9 subjects, from the most active channels on each subject, with actual oxy-data shown in blue colour and corresponding best fit shown in red colour. It is evident from Fig. 7 that the algorithm determined the best HRF with minimum error. The main concept of channel localization related to optode configuration is shown in Fig. 8. Let us consider a source (red cylinder) and a pair of detectors (grey cylinders). The NIR light path in between the source and each detector is supposed to be banana-shaped, with a depth of 50% of inter-source–detector distance. Suppose the second detector is placed 1 cm away from the first detector. Its corresponding channel shall be positioned near the first channel location with a depth difference of 0.5 cm. The two locations of the channels are shown with purple and blue circles, respectively, with a radial distance of z between them. Different layers of the head (scalp, skull, white matter, and grey matter) are shown in black-coloured lines. The scattered light that does not reach any detector is shown in green colour.

The 3 rectangular layers forming 24 channels and their corresponding depth differences from bottom ($Z = 1$) to top layer ($Z = 21$) and inter-layer ($Z = 11$) are shown in Fig. 9. The algorithm to estimate inter-channel activity-related patterns is shown in Fig. 10. The output of neuro-activation model is passed through the basic step to estimate the value of s depending on the minimization of GCV scores defined in Eq. (24). The next step is the determination of discrete cosine transform (DCT) of matrix X defined in Eq. (23). Finally, the inter-channel gap's
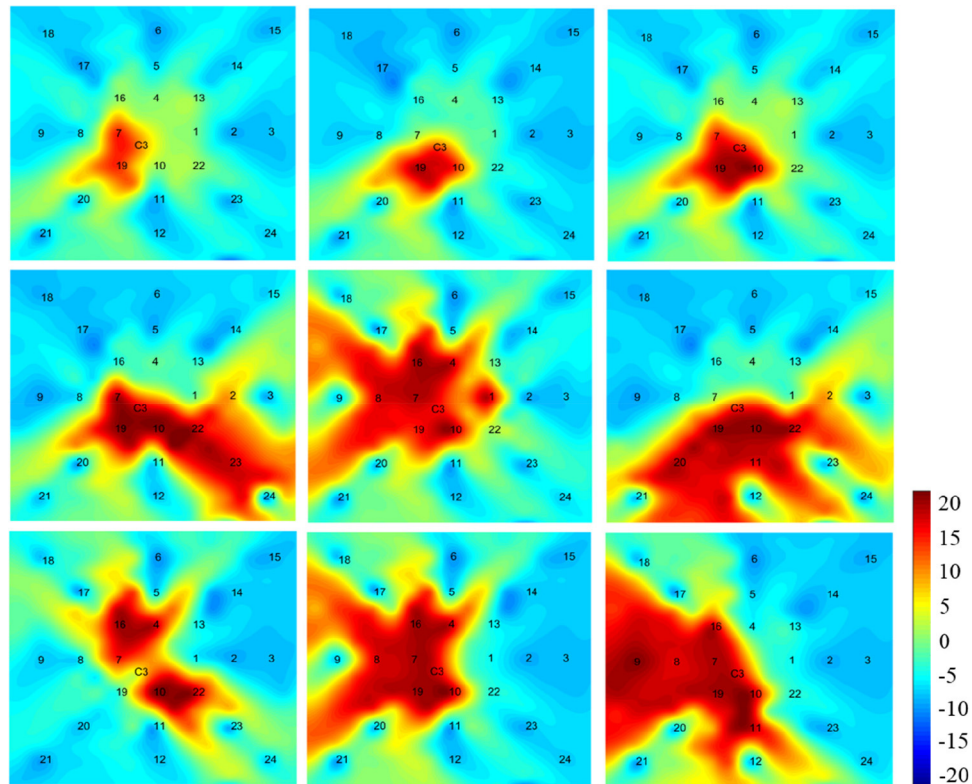
Fig. 5. Statistical t-maps of brain activation with fNIRS during finger-tapping task for all subjects (left to right, respectively). The channel locations are displayed as text numbers. The more activated areas and the channels are displayed in red colour, while the activity of inter-channel locations are estimated through weighted average scheme. The colour bar (at the bottom-right) shows activity strength.

activity-related waveform is estimated through inverse DCT (IDCT). This algorithm evaluates an activation value corresponding to each voxel and at each time step. Figure 11 presents the results related to a rectangular cube shown at motor cortex, with three axes labelled X, Y, and Z. The local origin is shown as O(0, 0, 0). 3-D brain maps are generated for the whole rectangular cube at each voxel through 24 channel-location data observed at 3 rectangular layers, as shown in Fig. 2. The results corresponding to some of the slices related to these rectangular cubes are shown in magnified part 1 (X = 53, X = 105, Y = 160, Z = 1 and Z = 11) and part 2 (X = 53, X = 105, Y = 160, Z = 1, Z = 11 and Z = 21).

To show the best resolution results with depth, the 3-D map's specific layer activation patterns related to Z = 21 are shown in Fig. 12. Similarly, the results for depth activation maps related to Z = 11 are shown in Fig. 13 for six subjects and are estimated through the proposed algorithm. In addition, for better view and understanding, the results related to different layers (Z = 1, X = 53, X = 105, Y = 80) are presented in Figs. 14–17.
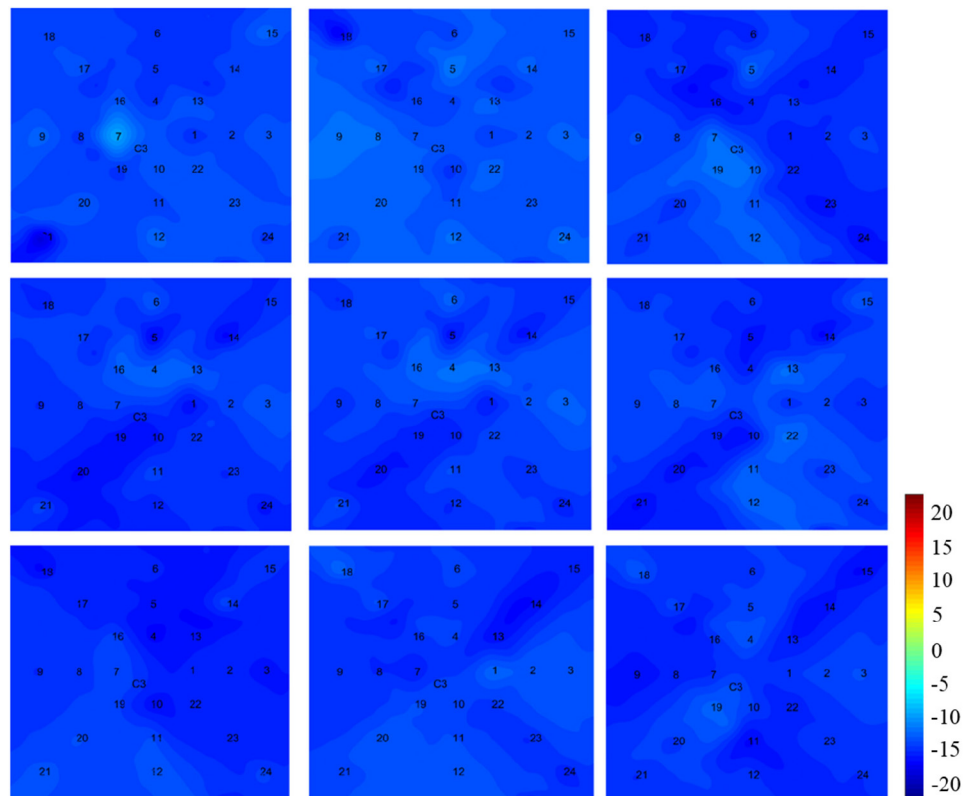
Biomedical Optics EXPRESS

Fig. 6. Statistical t-maps of brain activation with fNIRS during rest for nine subjects (left to right, respectively). The channel locations are displayed as text numbers, with the blue colour showing no activity. The colour bar (at the bottom-right) shows activity strength.
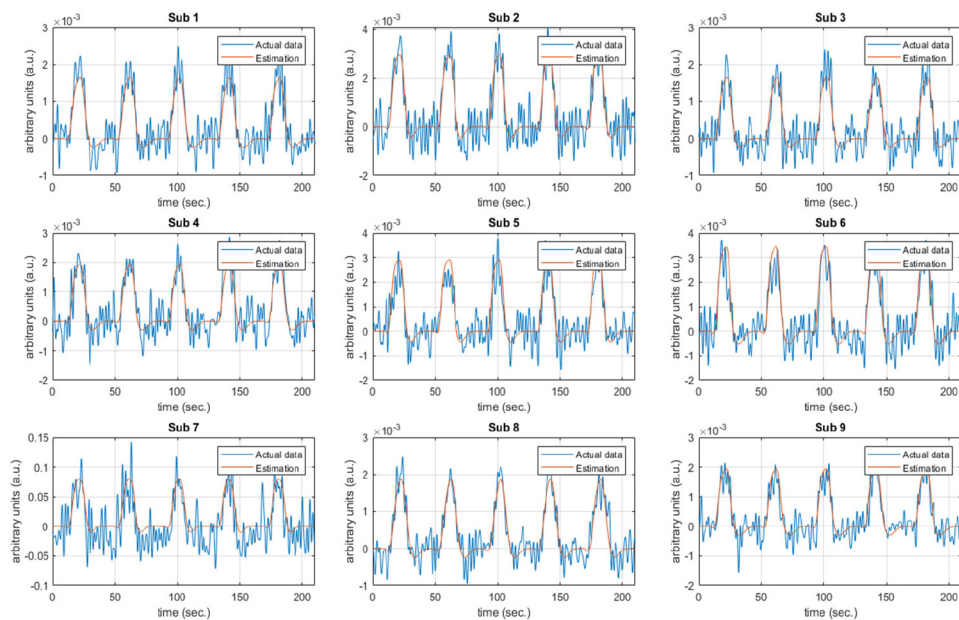
Fig. 7. Typical temporal waveforms of concentration changes in HbO$_2$ in different channels of each subject during the finger-tapping task. The real fNIRS data are represented by the blue-coloured waveform, while the estimated activation signal is represented by the red-coloured signal. The x-axis shows time, while the y-axis shows the relative concentration changes with arbitrary units.
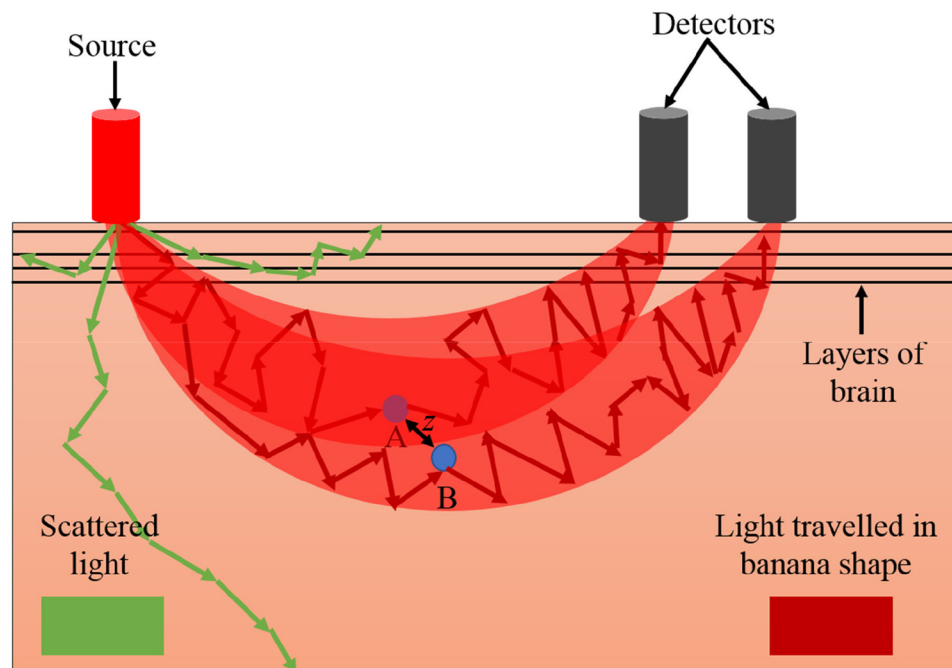
Fig. 8. Concept of measuring two supposed points (A and B) in brain with z distance apart, by shooting NIR light from source and detecting the NIR light from two detectors. The banana-shaped paths depict the travelling area of the NIR light photons, while the green-coloured arrows indicate the scattering. The red-coloured arrows show the extra distance travelled by photons, which is corrected by differential pathlength factor (DPF), while the black lines indicate the layers of the head.
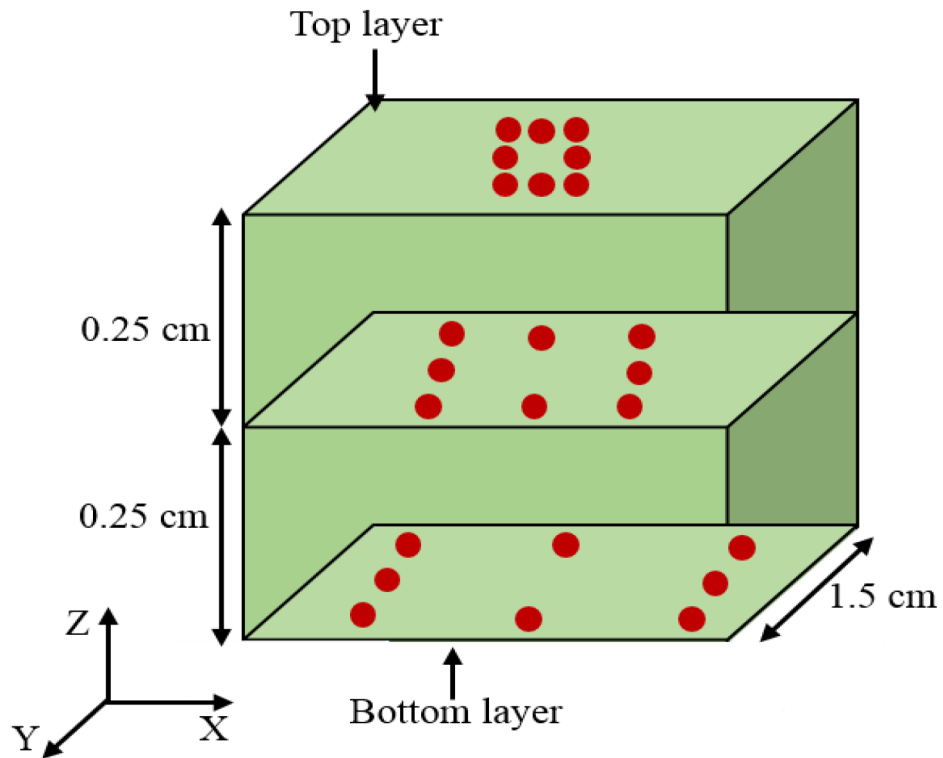
Fig. 9. Concept of the existence of channels at different layers of a supposed activated region, according to their distance from the source. The nearest channels lay at the top layer, the channels after that lay a little bit deeper at the middle layer, while the channels at the end of the configuration lay at the bottom layer of the activated region. The depth of the middle layer is 0.25 cm, making the region for analysis have dimensions of 0.5 cm × 1.5 cm × 1.5 cm.
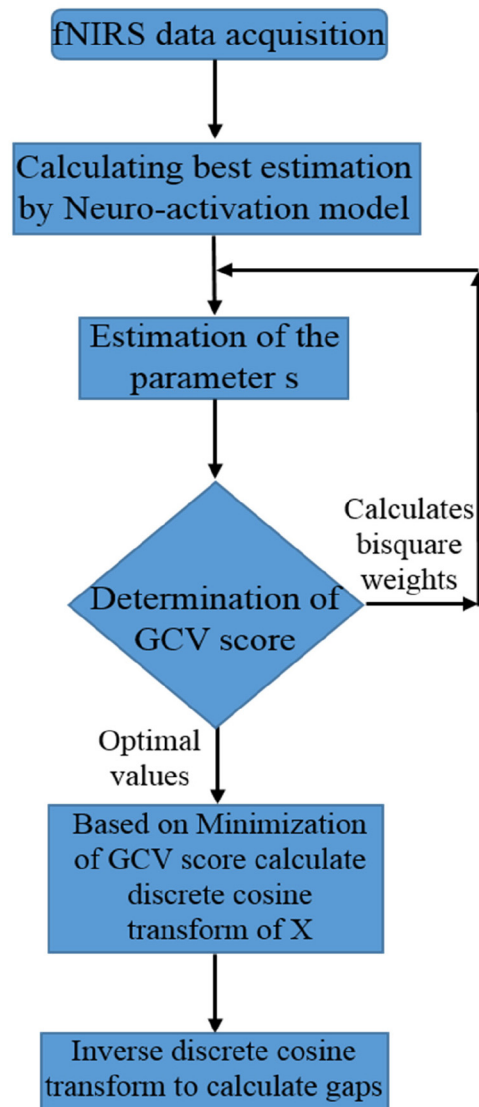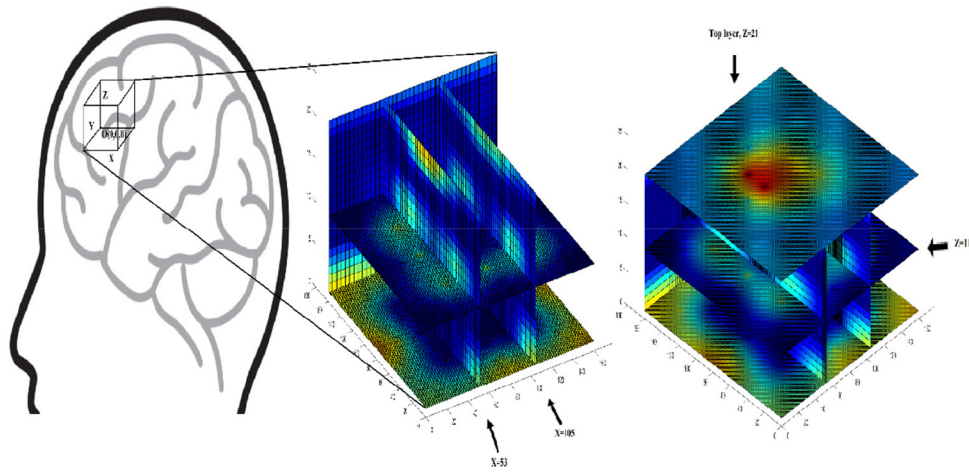
Fig. 10. Flow chart of algorithm.

Fig. 11. Sample figure of 3-D automatic estimation measured by proposed algorithm with different layers for subject 1. Layer-wise estimation for six subjects (1, 2, 4, 6, 8, 9) are shown in the next figures separately. (a) Pixel-wise automatic filling of activation gaps with different layers at X = 53, X = 105, Y = 161, and Z = 11. (b) Top view of activation at Z = 21.
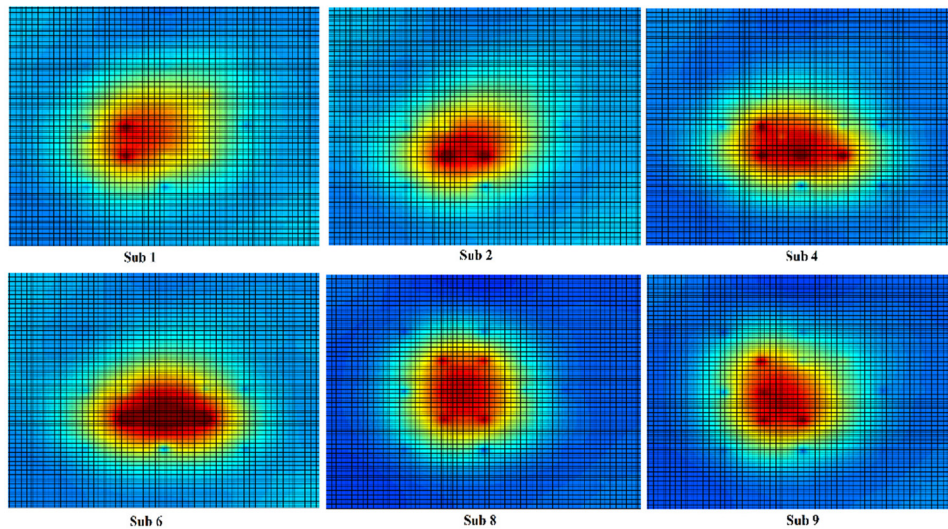

Fig. 12. Functional image of a particular slice at Z = 21 (top layer) separated from 3-D image acquired through proposed scheme shown in Fig. 11. This image includes activation related to only those channels which lie on the top layer of Fig. 9; activation related to other deep channels are not shown in this layer. The dark red colour shows the most activated areas with high resolution.
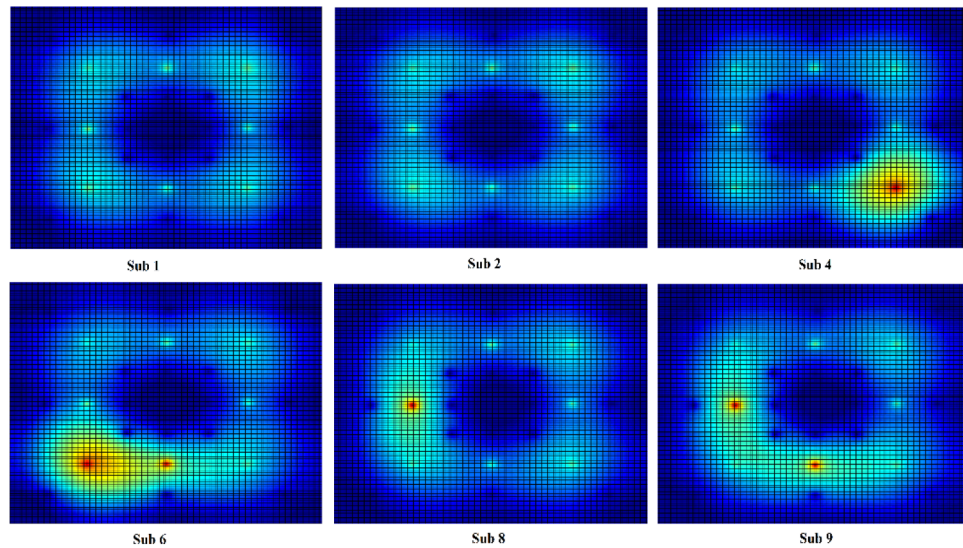
Fig. 13. Functional image of a particular slice at Z = 11 (middle layer) separated from 3-D image acquired through proposed scheme shown in Fig. 11. This image includes activation related to only those channels which lie on the middle layer of Fig. 9; activation related to other channels are not shown in this layer. The dark red colour shows the most activated areas with high resolution.

Fig. 14. Functional image of a particular slice at Z = 1 (bottom layer) separated from 3-D image acquired through proposed scheme shown in Fig. 11. This image includes activation related to only those channels which lie on the bottom layer of Fig. 9; activation related to other channels are not shown in this layer. The dark red colour shows the most activated areas with high resolution.
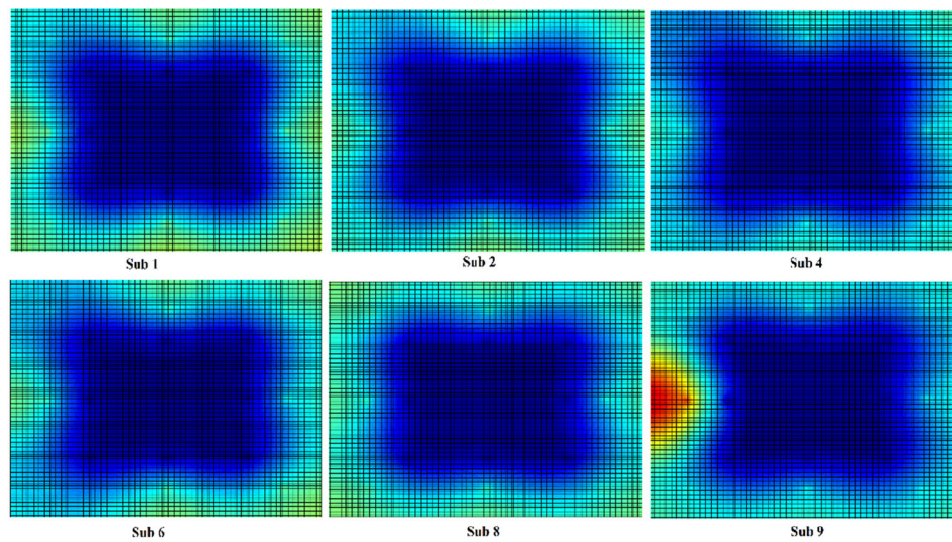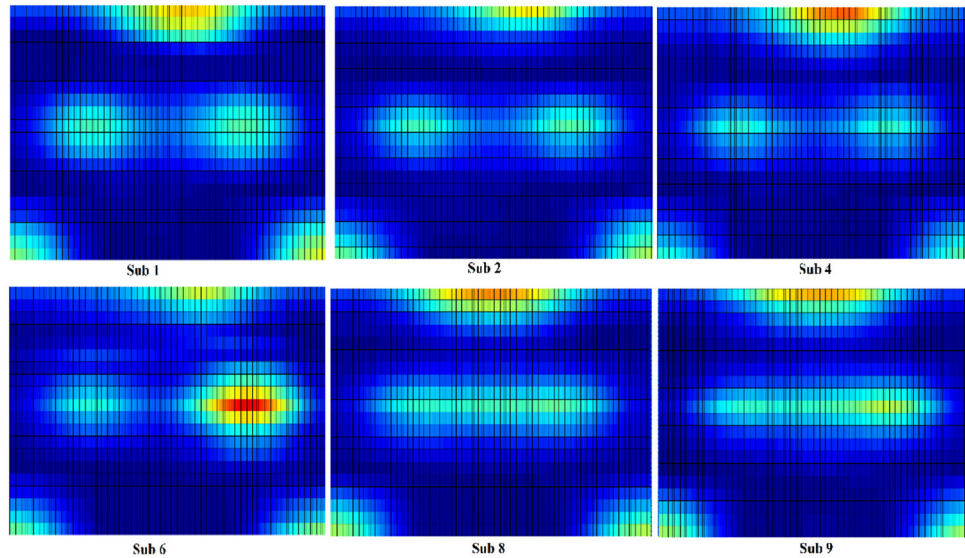
Fig. 15. Functional image of a particular slice at X = 53 separated from 3-D image acquired through proposed scheme shown in Fig. 11. This image includes activation related to only those channels which lie on X = 53 layer; activation related to other volume is not shown in this layer. The dark red colour shows the most activated areas with high resolution.
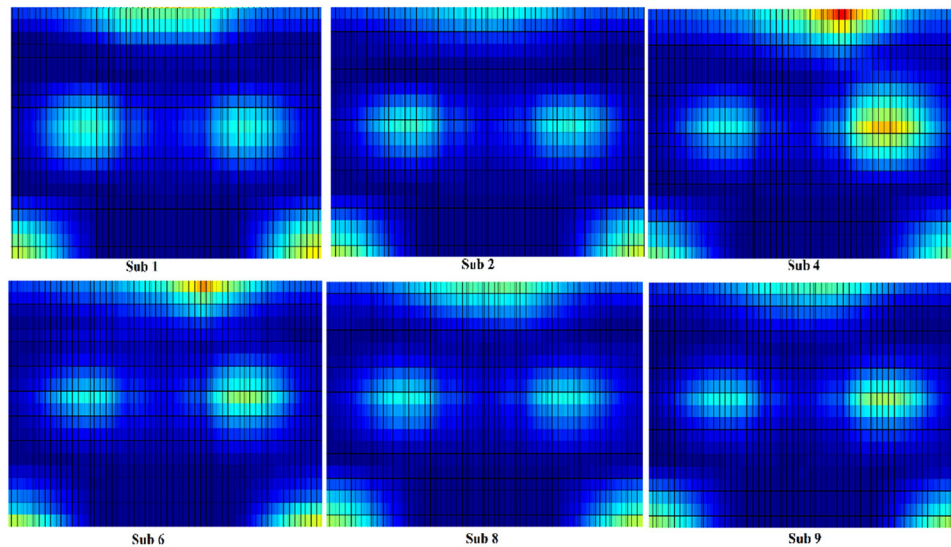
Fig. 16. Functional image of a particular slice at X = 105 separated from 3-D image acquired through proposed scheme shown in Fig. 11. This image includes activation related to only those channels which lie on X = 105 layer; activation related to other volume is not shown in this layer. The dark red colour shows the most activated areas with high resolution.

Fig. 17. Functional image of a particular slice at Y = 80 separated from 3-D image acquired through proposed scheme shown in Fig. 11. This image includes activation related to only those channels which lie on Y = 80 layer; activation related to other volume is not shown in this layer. The dark red colour shows the most activated areas with high resolution.
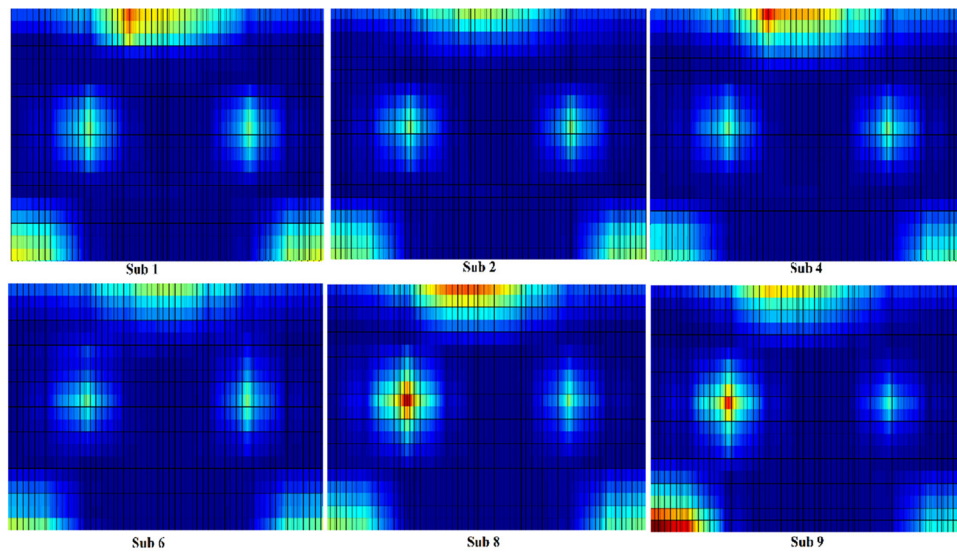
4. Discussion

Among OBI methodologies, fNIRS is at a favourable position in the examination of human neural activation. This feature attracts several researchers working in the design field into developing an advanced instrument for fNIRS. However, there are still several issues that need attention and research, e.g., sensitivity, depth accuracy, and spatial resolution [3]. DOI can possibly attain a spatial resolution of a few centimetres but decreases instantaneously with increasing depth in the brain [62]. These methodologies use non-overlapping probe configurations and thus have a spatial resolution no better than the centimetre scale [3]. Importantly, in terms of the depth axis, the spatial resolution in adult humans is inferior because of the hardness of the skull and the distance between source and detector (< 4 cm) [63]. In new-born babies, it is possible to enhance the depth resolution by measuring the transmission of NIR light; however, in adult humans, this is generally not possible [64]. The information gathered through fNIRS optical signals is converted into interpretable form through functional brain image. In reality, the basic idea (Fig. 8) is that the NIR light of dual wavelength is thrown on the scalp by the source (red cylinder). Let us assume we have configured two detectors (grey cylinders). Two channels formed as a result of this configuration having banana-shaped paths, which indicate the activation pattern at positions A and B, respectively, with a radial distance of z. The spatial coordinates of A and B are now supposed to be the half of the source–detector separation (depth-wise) and a midpoint of the banana-shaped path horizontally. Conventionally, the information acquired through several channels could be displayed through 2-D functional image maps (t-maps). irrespective of depth information, as shown in Fig. 4. Only the channel locations have a specific activation pattern, and remaining pixels/voxels have no information regarding functionality. A generic and simple solution to this problem is to generate weighted-average activation information at the remaining pixels, as shown in Fig. 5. This solves the problem; however, the depth information is missing. and each of the channels at any depth location is cumulatively displayed on the 2-D pattern. The estimation of activation at each pixel/voxel and at relative depth is the focus of this study.

To enhance the sensitivity of optical brain activation and the accuracy of HRF, the development of signal processing methodologies that can discriminate the measured signals in time and space is mandatory [20]. Barbour et al. have argued that optical tomography produce low-spatial-resolution images and that artefacts and noises are expected with time-varying properties [65]. For time-varying reconstruction, Prince et al. have used space-estimation methodologies to differentiate respiratory rhythm, brain activation signal, and cardiac pulsation [66]. For filtration of systemic signal fluctuations from brain-activated optical data, Zhang et al. applied principal component analysis to evaluate principal spatial components of spatio-temporal covariance of pre-processed optical data [67–69].

Earlier, it was common practice to show brain maps through activation points and smoothing the data along the 2-D axis, as published by Franceschini et al. and Maki et al [70,71]. The resolution is comparable to source–detector separation, and quantitative accuracy is compromised because the obtained image is not an optimal solution of the inverse problem [72]. However, if we look at Fig. 5, we can see the simple averaging results of the data displayed in Fig. 4. However, from these figures, no one can estimate or determine the depth of these activation and the corresponding strength of activation on those layers (depth). It is evident from Fig. 11 that not only activation is estimated but its depth-related relative activation has been found and displayed. This is a novel approach and would be beneficial specifically for the fNIRS community and, in general, for OBI. There are only a few published examples of DOT images of brain haemodynamics, for example, in rodents [30,73], in new-born human babies [74], and in adult humans [38]. The advancement of true DOT for brain activation in humans would improve the image spatial resolution and quantitative accuracy over that of current interpolating back-projection methods.

The intensity of NIR light is fundamentally known to gradually decrease as the source–detector separation increases [63]. Additionally, the amplitude of the sensitivity, which bridges between the optical characteristics inside the skull and the intensity of the light received, is highly non-uniform in the reflectance measurement [16]. Therefore, this amplitude would be strong in the neighbouring locations of the source but weak in the deep layers. This situation leads towards the reconstruction of the image. In this study, we have 24 distinct activation points at different depths, depending on source–detector separation. However, there are no absolute or relative data available that indicate or estimate the haemodynamic response at those locations. It is nonetheless quite logical that activation of a healthy human brain would be very smooth around the strong activation area until and unless there is no other strong activation point in the neighbouring area [20]. Thus, reconstruction of a volume of cortical surfaces based on distinct and different 3-D points could result in better 3-D activation maps. In the past, different algorithms have been presented for such activation maps, e.g., regularization algorithms [75,76], among them is the popular method Tikhonove regularization, which is also known as L2-norm regularization [77]. It is used frequently because of its ease of implementation and robustness of solution. The limitation of this algorithm is that the L2-norm penalty results in an over-smooth solution. On the other hand, in the proposed algorithm, the activation between two activity points have been estimated based upon the value of smoothness parameter s.

If we analyse the source–detector-configuration-forming channels (Fig. 9) of this study, the channels are localized at 3 layers forming three xy-planes, following the concept drawn in Fig. 8. Each layer has 8 channels (with respect to the source–detector separation), and distance between each layer is 0.25 cm, with the top-layer channels at approximately 1.25 cm depth. The particular pixels missing in each layer are estimated through the proposed algorithm, resulting in an enhanced image of each layer. Further, inter-layered pixels have been estimated through the proposed algorithm, forming an enhanced and improved version of 3-D functional brain maps and having voxel information at each location of specific 3-D cube with high resolution.

We applied the proposed algorithm on the 9 subjects, with the results for 6 of these subjects (1, 2, 4, 6, 8, and 9) having been shown. If we closely look at Fig. 11 in comparison with Fig. 4, the former represents the brain maps (for the respective randomly selected subjects) of each layer in a specific volume, which cumulatively have patterns similar to those displayed in Fig. 4. Therefore, the proposed algorithm would be beneficial to the fNIRS community for localizing depth-wise brain activation. In addition, different volume layers in the xy-, yz-, and xz-planes of specific locations are presented in Figs. 12–17 with higher activation pixels. It can be easily observed in Fig. 12 that all randomly selected subjects have most of the activated channels in the first layer at around reference point C_3 of the specific volume (Fig. 11) because of the finger-tapping task and specific configuration. Meanwhile, some of these subjects (4, 6, 8, and 9) also have channels activated in the second layer. In Fig. 13, we can clearly see those active channels in a particular location (i.e., second layer) for respective subjects. Additionally, only subject 9, in contrast with other subjects, also has one channel active in the third layer. This additional activation is displayed in Fig. 14. The remaining Figs. 15, 16, and 17 show different views of activated channels of specific volume with respect to different layers at X = 53, X = 105, and Y = 80, respectively, for better understanding. Based upon the observations made in this study, it is therefore in the interest of time that, instead of projecting 2-D cumulative images of functional activation, a better approach would be to display an enhanced layer-wise image to infer correct information. It is worthy to mention that some of the subjects have shown activation in areas near C_3, for example, as shown in Figs. 4 and 5 (subjects 4, 5, 6, 8, and 9). However, because only one source has been utilized in our configuration (Fig. 2), limited activation points are detected. This issue could be improved by using high-density probe configuration. Another important aspect is that, because the results are obtained for different brain-layer slices, limited areas are activated, depending on the activation signal observed at each layer.

5. Conclusion

In this study, a novel algorithm to enhance the spatial information of cortical activity has been proposed for OBI. To the best of our knowledge, this is the first study that estimates inter-channel brain activation with high resolution. The proposed algorithm measures/determines the activation of inter-channel based on the neighbouring response of optical imaging data. The algorithm is based on the minimization of GCV scores and inverse discrete cosine transform. The results show that brain-functionality information with high resolution, including depth information, is achieved, in contrast with existing methodologies. Statistical analyses have also been implemented for the validation of brain-functionality results. The full 3-D brain map is made possible by implementing the proposed strategy and collecting cortical signals through a full head scan. This enables an individual to view the brain response of a particular slice through OBI data, as one can view through fMRI.

Funding

Disclosures

The authors declare no conflicts of interest.

References

1. H. Santosa, M. Jiyoun Hong, S.-P. Kim, and K.-S. Hong, "Noise reduction in functional near-infrared spectroscopy signals by independent component analysis," Rev. Sci. Instrum. **84**(7), 073106 (2013).
2. R. A. Khan, N. Naseer, N. K. Qureshi, F. M. Noori, H. Nazeer, and M. U. Khan, "fNIRS-based Neurorobotic Interface for gait rehabilitation," J. Neuroeng. Rehabilitation **15**(1), 7 (2018).
3. D. A. Boas, A. M. Dale, and M. A. Franceschini, "Diffuse optical imaging of brain activation: approaches to optimizing image sensitivity, resolution, and accuracy," NeuroImage **23**, S275–S288 (2004).
4. M. Ferrari and V. Quaresima, "A brief review on the history of human functional near-infrared spectroscopy (fNIRS) development and fields of application," NeuroImage **63**(2), 921–935 (2012).
5. A. Kleinschmidt, H. Obrig, M. Requardt, K.-D. Merboldt, U. Dirnagl, A. Villringer, and J. Frahm, "Simultaneous recording of cerebral blood oxygenation changes during human brain activation by magnetic resonance imaging and near-infrared spectroscopy," J. Cereb. Blood Flow Metab. **16**(5), 817–826 (1996).
6. J. Grandjean, A. Schroeter, I. Batata, and M. Rudin, "Optimization of anesthesia protocol for resting-state fMRI in mice based on differential effects of anesthetics on functional connectivity patterns," NeuroImage **102**, 838–847 (2014).
7. E. Jonckers, J. Van Audekerke, G. De Visscher, A. Van der Linden, and M. Verhoye, "Functional connectivity fMRI of the rodent brain: comparison of functional connectivity networks in rat and mouse," PLoS One **6**(4), e18876 (2011).
8. F. F. Jobsis, "Noninvasive, infrared monitoring of cerebral and myocardial oxygen sufficiency and circulatory parameters," Science **198**(4323), 1264–1267 (1977).
9. F. Scholkmann, S. Kleiser, A. J. Metz, R. Zimmermann, J. M. Pavia, U. Wolf, and M. Wolf, "A review on continuous wave functional near-infrared spectroscopy and imaging instrumentation and methodology," NeuroImage **85**, 6–27 (2014).
10. P. Pinti, I. Tachtsidis, A. Hamilton, J. Hirsch, C. Aichelburg, S. Gilbert, and P. W. Burgess, "The present and future use of functional near-infrared spectroscopy (fNIRS) for cognitive neuroscience," *Ann. N. Y. Acad. Sci.* (2018).
11. W. B. Baker, A. B. Parthasarathy, D. R. Busch, R. C. Mesquita, J. H. Greenberg, and A. Yodh, "Modified Beer-Lambert law for blood flow," Biomed. Opt. Express **5**(11), 4053–4075 (2014).
12. N. Roche-Labarbe, B. Zaaimi, P. Berquin, A. Nehlig, R. Grebe, and F. Wallois, "NIRS-measured oxy-and deoxyhemoglobin changes associated with EEG spike-and-wave discharges in children," Epilepsia **49**(11), 1871–1880 (2008).
13. S. Telkemeyer, S. Rossi, S. P. Koch, T. Nierhaus, J. Steinbrink, D. Poeppel, H. Obrig, and I. Wartenburger, "Sensitivity of newborn auditory cortex to the temporal structure of sounds," J. Neurosci. **29**(47), 14726–14733 (2009).
14. F. Homae, H. Watanabe, T. Nakano, K. Asakawa, and G. Taga, "The right hemisphere of sleeping infant perceives sentential prosody," Neurosci. Res. **54**(4), 276–280 (2006).
15. B. W. Zeff, B. R. White, H. Dehghani, B. L. Schlaggar, and J. P. Culver, "Retinotopic mapping of adult human visual cortex with high-density diffuse optical tomography," Proc. Natl. Acad. Sci. **104**(29), 12169–12174 (2007).

16. S. Brigadoi and R. J. Cooper, "How short is short? Optimum source–detector distance for short-separation channels in functional near-infrared spectroscopy," Neurophotonics **2**(2), 025005 (2015).

17. T. Wilcox and M. Biondi, "fNIRS in the developmental sciences," Wiley Interdisc. Rev. Cogn. Sci. **6**(3), 263–283 (2015).

18. E. Okada and D. T. Delpy, "Near-infrared light propagation in an adult head model. II. Effect of superficial tissue thickness on the sensitivity of the near-infrared spectroscopy signal," Appl. Opt. **42**(16), 2915–2921 (2003).

19. F. Orihuela-Espina, D. R. Leff, D. R. James, A. W. Darzi, and G.-Z. Yang, "Quality control and assurance in functional near infrared spectroscopy (fNIRS) experimentation," Phys. Med. Biol. **55**(13), 3701–3724 (2010).

20. D. Boas, K. Chen, D. Grebert, and M. Franceschini, "Improving the diffuse optical imaging spatial resolution of the cerebral hemodynamic response to brain activation in humans," Opt. Lett. **29**(13), 1506–1508 (2004).

21. C. Issard and J. Gervain, "Variability of the hemodynamic response in infants: Influence of experimental design and stimulus complexity," Developmental cognitive neuroscience **33**, 182–193 (2018).

22. D. T. Delpy, M. Cope, P. van der Zee, S. Arridge, S. Wray, and J. Wyatt, "Estimation of optical pathlength through tissue from direct time of flight measurement," Phys. Med. Biol. **33**(12), 1433–1442 (1988).

23. M. S. Patterson, B. Chance, and B. C. Wilson, "Time resolved reflectance and transmittance for the noninvasive measurement of tissue optical properties," Appl. Opt. **28**(12), 2331–2336 (1989).

24. D. Delpy and M. Cope, "Quantification in tissue near–infrared spectroscopy," Philos. Trans. R. Soc., B **352**(1354), 649–659 (1997).

25. A. Bakker, B. Smith, P. Ainslie, and K. Smith, "Near-infrared spectroscopy," in *Applied Aspects of Ultrasonography in Humans* (InTech, 2012).

26. B. Chance, S. Nioka, J. Kent, K. McCully, M. Fountain, R. Greenfeld, and G. Holtom, "Time-resolved spectroscopy of hemoglobin and myoglobin in resting and ischemic muscle," Anal. Biochem. **174**(2), 698–707 (1988).

27. M. Oda, Y. Yamashita, G. Nishimura, and M. Tamura, "A simple and novel algorithm for time-resolved multiwavelength oximetry," Phys. Med. Biol. **41**(3), 551–562 (1996).

28. B. Chance, M. B. Maris, J. Sorge, and M. Zhang, "Phase modulation system for dual wavelength difference spectroscopy of hemoglobin deoxygenation in tissues," Proc. SPIE **1204**, 481–492 (1990).

29. B. W. Pogue, T. O. McBride, J. Prewitt, U. L. Osterberg, and K. D. Paulsen, "Spatially variant regularization improves diffuse optical tomography," Appl. Opt. **38**(13), 2950–2961 (1999).

30. J. P. Culver, T. Durduran, T. Furuya, C. Cheung, J. H. Greenberg, and A. G. Yodh, "Diffuse optical tomography of cerebral blood flow, oxygenation, and metabolism in rat during focal ischemia," J. Cereb. Blood Flow Metab. **23**(8), 911–924 (2003).

31. H. Dehghani, B. R. White, B. W. Zeff, A. Tizzard, and J. P. Culver, "Depth sensitivity and image reconstruction analysis of dense imaging arrays for mapping brain function with diffuse optical tomography," Appl. Opt. **48**(10), D137–D143 (2009).

32. H. J. Niu, F. H. Tian, Z. J. Lin, and H. L. Liu, "Development of a compensation algorithm for accurate depth localization in diffuse optical tomography," Opt. Lett. **35**(3), 429–431 (2010).

33. A. K. Singh, M. Okamoto, H. Dan, V. Jurcak, and I. Dan, "Spatial registration of multichannel multi-subject fNIRS data to MNI space without MRI," NeuroImage **27**(4), 842–851 (2005).

34. A. T. Eggebrecht, B. R. White, S. L. Ferradal, C. X. Chen, Y. X. Zhan, A. Z. Snyder, H. Dehghani, and J. P. Culver, "A quantitative spatial comparison of high-density diffuse optical tomography and fMRI cortical mapping," NeuroImage **61**(4), 1120–1128 (2012).

35. T. Yamamoto, A. Maki, T. Kadoya, Y. Tanikawa, Y. Yamada, E. Okada, and H. Koizumi, "Arranging optical fibres for the spatial resolution improvement of topographical images," Phys. Med. Biol. **47**(18), 3429–3440 (2002).

36. E. Okada, M. Firbank, M. Schweiger, S. R. Arridge, M. Cope, and D. T. Delpy, "Theoretical and experimental investigation of near-infrared light propagation in a model of the adult head," Appl. Opt. **36**(1), 21–31 (1997).

37. X. Cui, S. Bray, and A. L. Reiss, "Functional near infrared spectroscopy (NIRS) signal improvement based on negative correlation between oxygenated and deoxygenated hemoglobin dynamics," NeuroImage **49**(4), 3039–3046 (2010).

38. A. Y. Bluestone, G. Abdoulaev, C. H. Schmitz, R. L. Barbour, and A. H. Hielscher, "Three-dimensional optical tomography of hemodynamics in the human head," Opt. Express **9**(6), 272–286 (2001).

39. M. J. Diamantopoulou, "Filling gaps in diameter measurements on standing tree boles in the urban forest of Thessaloniki, Greece," Environ. Modell. Softw. **25**(12), 1857–1865 (2010).

40. A. Alvera-Azcarate, A. Barth, J. M. Beckers, and R. H. Weisberg, "Multivariate reconstruction of missing data in sea surface temperature, chlorophyll, and wind satellite fields (vol 112, art no C03008, 2007)," J. Geophys. Res.: Oceans **112**(C3), C03008 (2007).

41. D. Kondrashov and M. Ghil, "Spatio-temporal filling of missing points in geophysical data sets," Nonlinear. Proc. Geoph. **13**(2), 151–159 (2006).

42. K. Hocke and N. Kampfer, "Gap filling and noise reduction of unevenly sampled data by means of the Lomb-Scargle periodogram," Atmos. Chem. Phys. **9**(12), 4197–4206 (2009).

43. Y. Hoshi and M. Tamura, "Fluctuations in the cerebral oxygenation state during the resting period in functional mapping studies of the human brain," Med. Biol. Eng. Comput. **35**(4), 328–330 (1997).

44. V. Toronov, M. A. Franceschini, M. Filiaci, S. Fantini, M. Wolf, A. Michalos, and E. Gratton, "Near-infrared study of fluctuations in cerebral hemodynamics during rest and motor stimulation: Temporal analysis and spatial mapping," Med. Phys. **27**(4), 801–815 (2000).

45. J. C. Ye, S. Tak, K. E. Jang, J. Jung, and J. Jang, "NIRS-SPM: statistical parametric mapping for near-infrared spectroscopy," NeuroImage **44**(2), 428–447 (2009).

46. T. Fekete, D. Rubin, J. M. Carlson, and L. R. Mujica-Parodi, "The NIRS analysis package: noise reduction and statistical inference," PLoS One **6**(9), e24322 (2011).

47. M. A. Kamran, N. Mannan, M. Muhammad, and M. Y. Jeong, "Initial-dip existence and estimation in relation to DPF and data drift," Front. Neuroinform. **12**, 96 (2018).

48. M. A. Kamran, M. Y. Jeong, and M. Mannan, "Optimal hemodynamic response model for functional near-infrared spectroscopy," Front. Behav. Neurosci. **9**, 151 (2015).

49. A. F. Abdelnour and T. Huppert, "Real-time imaging of human brain function by near-infrared spectroscopy using an adaptive general linear model," NeuroImage **46**(1), 133–143 (2009).

50. M. A. Kamran, M. M. N. Mannan, and M. Y. Jeong, "Initial-Dip Existence and Estimation in Relation to DPF and Data Drift," Front. Neuroinform. **12**, 96 (2018).

51. R. B. Buxton, K. Uludag, D. J. Dubowitz, and T. T. Liu, "Modeling the hemodynamic response to brain activation," NeuroImage **23**, S220–S233 (2004).

52. K. Yoshino and T. Kato, "Vector-based phase classification of initial dips during word listening using near-infrared spectroscopy," NeuroReport **23**(16), 947–951 (2012).

53. J. C. Lagarias, J. A. Reeds, M. H. Wright, and P. E. Wright, "Convergence properties of the Nelder-Mead simplex method in low dimensions," SIAM J. Control **9**(1), 112–147 (1998).

54. M. A. Luersen and R. Le Riche, "Globalized Nelder-Mead method for engineering optimization," Comput. Struct. **82**(23-26), 2251–2260 (2004).

55. X. S. Hu, K. S. Hong, S. Z. S. Ge, and M. Y. Jeong, "Kalman estimator- and general linear model-based on-line brain activation mapping by near-infrared spectroscopy," Biomed. Eng. Online **9**(1), 82 (2010).

56. D. Garcia, "Robust smoothing of gridded data in one and higher dimensions with missing values," Comput. Stat. Data An. **54**(4), 1167–1178 (2010).

57. G. Strang, "The discrete cosine transform," SIAM Rev. **41**(1), 135–147 (1999).

58. G. J. Wang, D. Garcia, Y. Liu, R. de Jeu, and A. J. Dolman, "A three-dimensional gap filling method for large geophysical datasets: Application to global satellite soil moisture observations," Environ. Modell. Softw. **30**, 139–142 (2012).

59. P. H. C. Eilers, "A perfect smoother," Anal. Chem. **75**(14), 3631–3636 (2003).

60. H. L. Weinert, "Efficient computation for Whittaker-Henderson smoothing," Comput. Stat. Data An. **52**(2), 959–974 (2007).

61. M. A. Kamran, N. Mannan, M. Muhammad, and M. Y. Jeong, "Differential path-length factor's effect on the characterization of brain's hemodynamic response function: a functional near-infrared study," Front. Neuroinform. **12**, 37 (2018).

62. M. Caffini, D. Contini, R. Re, L. M. Zucchelli, R. Cubeddu, A. Torricelli, and L. Spinelli, "Functional near infrared spectroscopy and diffuse optical tomography in neuroscience," in *Advances in Brain Imaging* (IntechOpen, 2012).

63. Y. Hoshi and F. Michael, "Functional near-infrared spectroscopy: potential and limitations in neuroimaging studies," Int. Rev. Neurobiol. **66**, 237–266 (2005).

64. S. R. Hintz, W.-F. Cheong, J. P. Van Houten, D. K. Stevenson, and D. A. Benaron, "Bedside imaging of intracranial hemorrhage in the neonate using light: comparison with ultrasound, computed tomography, and magnetic resonance imaging," Pediatr. Res. **45**(1), 54–59 (1999).

65. R. L. Barbour, H. L. Graber, Y. Pei, S. Zhong, and C. H. Schmitz, "Optical tomographic imaging of dynamic features of dense-scattering media," J. Opt. Soc. Am. A **18**(12), 3018–3036 (2001).

66. S. Prince, V. Kolehmainen, J. P. Kaipio, M. A. Franceschini, D. Boas, and S. R. Arridge, "Time-series estimation of biological factors in optical diffusion tomography," Phys. Med. Biol. **48**(11), 1491–1504 (2003).

67. Q. Zhang, E. N. Brown, and G. E. Strangman, "Adaptive filtering for global interference cancellation and real-time recovery of evoked brain activity: a Monte Carlo simulation study," J. Biomed. Opt. **12**(4), 044014 (2007).

68. Q. Zhang, E. N. Brown, and G. E. Strangman, "Adaptive filtering to reduce global interference in evoked brain activity detection: a human subject case study," J. Biomed. Opt. **12**(6), 064009 (2007).

69. Q. Zhang, G. E. Strangman, and G. Ganis, "Adaptive filtering to reduce global interference in non-invasive NIRS measures of brain activation: how well and when does it work?" NeuroImage **45**(3), 788–794 (2009).

70. A. Maki, Y. Yamashita, Y. Ito, E. Watanabe, Y. Mayanagi, and H. Koizumi, "Spatial and temporal analysis of human motor activity using noninvasive NIR topography," Med. Phys. **22**(12), 1997–2005 (1995).

71. M. A. Franceschini, V. Toronov, M. E. Filiaci, E. Gratton, and S. Fantini, "On-line optical imaging of the human brain with 160-ms temporal resolution," Opt. Express **6**(3), 49–57 (2000).

72. S. R. Arridge, "Optical tomography in medical imaging," Inverse Problems **15**(2), R41–R93 (1999).

73. A. Siegel, J. Marota, and D. A. Boas, "Design and evaluation of a continuous-wave diffuse optical tomography system," Opt. Express **4**(8), 287–298 (1999).

74. S. R. Hintz, D. A. Benaron, A. M. Siegel, A. Zourabian, D. K. Stevenson, and D. A. Boas, "Bedside functional imaging of the premature infant brain during passive motor activation," J. Perinat. Med. **29**(4), 335–343 (2001).

75. W. Lu, D. Lighter, and I. B. Styles, "L 1-norm based nonlinear reconstruction improves quantitative accuracy of spectral diffuse optical tomography," Biomed. Opt. Express **9**(4), 1423–1444 (2018).

76. J. Yao, F. Tian, Y. Rakvongthai, S. Oraintara, and H. Liu, "Quantification and normalization of noise variance with sparsity regularization to enhance diffuse optical tomography," Biomed. Opt. Express **6**(8), 2961–2979 (2015).

77. T. Shimokawa, T. Kosaka, O. Yamashita, N. Hiroe, T. Amita, Y. Inoue, and M.-a. Sato, "Hierarchical Bayesian estimation improves depth accuracy and spatial resolution of diffuse optical tomography," Opt. Express **20**(18), 20427–20446 (2012).